Analysis of Asymmetric Disk-Shaped and Flat-Plate Heat Pipes

K. Vafai
Professor.
Fellow ASME

N. Zhu

Department of Mechanical Engineering,
The Ohio State University,
Columbus, OH 43210

W. Wang
CETE, College of Education,
The Ohio State University,
Columbus, OH 43210

An analytical investigation and conceptual design of a disk-shaped asymmetric heat pipe is presented in this work. Using the conservative formulations for the steady incompressible vapor and liquid flow for a disk-shaped heat pipe, an in-depth integral analysis is applied. Analytical results for the asymmetric vapor velocity profile, the vapor and liquid pressure distributions, and the vapor temperature distribution in the heat pipe are obtained and compared to those of rectangular flat-plate heat pipe. The analysis establishes the physics of the process and the intrawick interactions for the disk-shaped heat pipe. The effects of variations in the thicknesses of the vapor channel and the wick as well as the heat pipe on the performance of both disk-shaped and rectangular flat-plate heat pipes are analyzed in detail and compared with each other. The factors limiting heat pipe performance are discussed and the results show that the disk-shaped heat pipe, while utilizing a smaller surface area and being more adaptable to several application areas, significantly increases the heat transfer capability per unit surface area compared to rectangular flat-plate heat pipe.

Introduction

Heat pipes have been studied extensively in the last three decades. Almost all of the studies, both numerical and experimental, have focused on the operation and performance of cylindrical heat pipes or concentric annular heat pipes having a symmetric heat source and sink (Tien, 1975; Winter and Barsch, 1971; Faghri, 1986). While theoretical bases of these symmetric heat pipes have been well established for a wide variety of application areas, the application of heat pipes to asymmetric heat sources and the investigation of asymmetric heat pipes has been mostly neglected.

Ooijen and Hoogendoorn (1979) studied the vapor flow numerically in a flat-plate heat pipe with adiabatic top wall. Assuming the same injection and suction velocity, they solved the momentum equations for steady laminar incompressible two-dimensional vapor flow using a finite-difference method. In their work no change of phase was involved and the wick and the liquid flow were neglected. Vafai and Wang (1992) investigated the operation and overall performance of an asymmetric rectangular flat-plate heat pipe using a detailed integral analysis. The study was based on steady, incompressible vapor and liquid flow with pseudo-three-dimensional vapor flow field bifurcated on the $x-y$ plane due to the asymmetric nature of heat source and sinks. The analytical results for the shifted vapor velocity profiles on the $x-y$ plane, the overall axial pressure distributions in both vapor and liquid phases, and the axial vapor temperature distribution in the heat pipe were obtained. The good qualitative agreement between the results obtained and those based on the solution of the field equations for the conventional symmetric cases (Dunn and Reay, 1982; Ivanovskii et al., 1982) and asymmetric case (Ooijen and Hoogendoorn, 1979) demonstrated that the in-depth integral method provides accurate results on modeling the flow and heat transfer characteristics of asymmetric flat plate heat pipes.

Compared to the rectangular flat-plate heat pipe the disk-shaped heat pipe is more adaptable to several application areas due to its geometry and smaller surface area. Maezawa et al. (1981) studied the heat transfer characteristics of a disk-shaped rotating, wickless heat pipe. They concentrated their study on the condensate layer and found the condensate velocity distribution by establishing the force balance within the condensate layer. Having no wick in the heat pipe and utilizing centrifugal forces for condensate return, they applied Nusselt's theory of laminar film condensation to the condensate layer and obtained the heat transfer rate by assuming a linear temperature distribution within the condensate film. In their study the disk-shaped heat pipe is considered to be a special type of rotating heat pipe with symmetric heat source and sink.

In the present work the vapor and liquid flow in a disk-shaped heat pipe heated asymmetrically, the overall heat pipe performance, as well as the conceptual design are investigated analytically. Using the conservative formulations for the steady incompressible vapor and liquid flow in the heat pipe, an in-depth integral analysis is employed to obtain the velocity profiles and overall pressure distributions for both vapor and liquid phases. The heat transfer capability for different sizes of the disk-shaped heat pipe is obtained based on the capillary limit and is compared with that of the rectangular flat-plate heat pipe proposed by Vafai and Wang (1992). The effects of variations in the thickness of the wick and the vapor channel as well as the overall thickness of the heat pipe on the performance of both disk-shaped and rectangular flat-plate heat pipes are analyzed and compared to each other.

A specific application will be considered for the disk-shaped heat pipe used in our analysis, namely, Boron Neutron Capture Therapy (BNCT), which has an important medical application. A description of this application is given in the literature (Vafai and Wang, 1992). The disk-shaped heat pipe, with heavy water as working fluid, is more suitable for the BNCT application than the rectangular flat-plate heat pipe due to its size, geometry, and thermal performance and will be used to remove the high heat flux generated by the proton bombardments of the lithium target. However, it should be noted that all of the analytical results are completely general and apply to various configurations of both symmetric and asymmetric disk-shaped heat pipes.

Analysis and Formulation

The schematic diagram of the heat pipe under study is shown in Fig. 1. The heat generated from the proton bombardment of the lithium target is imposed on a portion of the bottom part of

Contributed by the Heat Transfer Division for publication in the JOURNAL OF HEAT TRANSFER. Manuscript received by the Heat Transfer Division August 1993; revision received April 1994. Keywords: Augmentation and Enhancement, Heat Pipes and Thermosyphons, Phase-Change Phenomena. Associate Technical Editor: A. Faghri.

the heat pipe and causes the vaporization and subsequent pressurization of the liquid in the wick. Part of the vapor is condensed on the opposite surface of the evaporator; however, most of it is condensed downstream of the evaporator. The vapor space is divided into several channels by vertical wicks, which transport liquid from the upper wick to the lower wick. Any one of the internal channels can be considered as a building block for the disk-shaped heat pipe. Therefore, we will concentrate on the fluid flow considerations within one of these channels (Fig. 1*b*). Once the fluid flow characteristics within one of the channels are determined, the fluid flow characteristics of the entire heat pipe can be easily established. The results of this analysis are applicable to any number of channels, any specified thickness of the wick, as well as any specified thickness of the disk-shaped heat pipe.

In our analysis the position coordinates, velocities, pressures, and temperature are nondimensionalized by $h^2 v_1/\nu_v$, h, Φ, v_1, ν_v/h, $\rho_v v_1^2$, and $h_{fg}/\bar{R}$, where ν_v is the vapor kinematic viscosity, v_1 is the vapor injection velocity, which is related to the input power through $v_1 = Q/\rho_v A_e h_{fg}$, ρ_v is the vapor density, h and Φ are the height and angle of the vapor space for any one of the vapor flow channels, h_{fg} is the latent heat of the working fluid, and $\bar{R}$ is the ideal gas constant.

In the heat pipe research performed to date, researchers have made some traditional assumptions in modeling and analysis. An important assumption made by various researchers is that the capillary porous wick is always saturated with liquid phase working fluid and vapor flows only in the core region during the operation of the heat pipe. Hence, evaluation of the effective thermal conductivity and formulation of the capillary pressure were simplified. This assumption will be employed in the present investigation. We will also make the following common assumptions, which are usually made in analyzing the heat pipes:

1 Vapor and liquid flow are steady, laminar, and subsonic.
2 Transport properties for the vapor and liquid are taken as constants.
3 The vapor injection and suction rate are uniform in the evaporator and condenser sections.
4 The vapor velocity component in the θ direction is negligible since the injection and suction on the vertical wicks are negligible. However, the θ component of the liquid velocity is considered in the analysis.

1 Vapor Phase Analysis. Based on these assumptions, the continuity Eq. (1) and the r-direction momentum Eq. (2) govern the vapor flow

$$\frac{\partial u_v^+}{\partial r^+} + \frac{\partial v_v^+}{\partial y^+} + \frac{u_v^+}{r^+} = 0 \tag{1}$$

$$u_v^+ \frac{\partial u_v^+}{\partial r^+} + v_v^+ \frac{\partial u_v^+}{\partial y^+} = -\frac{\partial p_v^+}{\partial r^+} + \frac{1}{\mathrm{Re}_h^2}\left[\frac{\partial^2 u_v^+}{\partial (r^+)^2} + \frac{1}{r^+}\frac{\partial u_v^+}{\partial r^+} - \frac{u_v^+}{(r^+)^2} + \mathrm{Re}_h^2 \frac{\partial^2 u_v^+}{\partial (y^+)^2} + \frac{1}{\Phi^2 (r^+)^2}\frac{\partial^2 u_v^+}{\partial (\theta^+)^2}\right] \tag{2}$$

In these equations $\mathrm{Re}_h = v_1 h/\nu_v$ is defined as the injection Reynolds number. The associated boundary conditions of the problem are

$$u_v^+(r^+, y^+, 0) = u_v^+(r^+, y^+, 1) = 0 \tag{3}$$

$$u_v^+(r^+, 0, \theta^+) = u_v^+(r^+, 1, \theta^+) = 0 \tag{4}$$

$$u_v^+(0, y^+, \theta^+) = u_v^+(R^+, y^+, \theta^+) = 0 \tag{5}$$

$$v_v^+(r^+, 0, \theta^+) = -v_2^+,$$

$$v_v^+(r^+, 1, \theta^+) = \begin{cases} -v_1^+ & (0 \le r^+ \le \varphi R^+) \\ +v_2^+ & (\varphi R^+ \le r^+ \le R^+), \end{cases} \tag{6}$$

As indicated in Eq. (6), within the $0 \le r^+ \le \varphi R^+$ region, the lower wick acts as the evaporator and the upper wick as the condenser. However, both upper and lower wicks act as condensers within the $\varphi R^+ \le r^+ \le R^+$ region. The parameter φ will be established later.

(a) Velocity Profile. Based on the numerical results given by Narayana (1986), Faghri (1986), and Sorour et al. (1987), a parabolic velocity profile will be used for vapor flow within the heat pipe. The dimensionless velocity profile $u_v^+(r^+, y^+, \theta^+)$ will be represented by a functional product in the r^+, y^+, and θ^+ directions; that is

$$u_v^+(r^+, y^+, \theta^+) = U_v^+(r^+)[a_0 + a_1 y^+ + a_2 (y^+)^2] \times [c_0 + c_1\theta^+ + c_2(\theta^+)^2] \tag{7}$$

where $U_v^+(r^+)$ denotes the maximum velocity for $u_v^+(r^+, y^+, \theta^+)$ on every transverse surface along the r^+ axis. Because of the symmetric conditions in the θ^+ direction (i.e., boundary conditions (3)), the constants c_0, c_1, and c_2 for the θ^+ component of $u_v^+(r^+, y^+, \theta^+)$ are easily specified as

$$[c_0 + c_1\theta^+ + c_2(\theta^+)^2] = 4\theta^+(1 - \theta^+) \tag{8}$$

Nomenclature

A_e = evaporator area, m^2
A_{total} = total external surface area of the heat pipe, m^2
$f(r)$ = location of the maximum vapor velocity, m
$f^+(r^+)$ = dimensionless location of the maximum vapor velocity
h = height of vapor space for the heat pipe, m
h_{fg} = latent heat of working fluid, kJ/kg
h_{total} = thickness of the heat pipe = $h + 2h_w$, m
h_w = thickness of the wick, m
h_w^+ = dimensionless thickness of the wick = h_w/h
K = permeability, m^2
K^+ = dimensionless permeability = K/h_w^2
k_e = effective thermal conductivity of the liquid-saturated wick, W/mK
p_0 = saturation pressure, Pa
p_l = liquid pressure, Pa
p_v = vapor pressure, Pa
p_l^+ = dimensionless liquid pressure = $p_l/\rho_l v_1^2$
p_v^+ = dimensionless vapor pressure = $p_v/\rho_v v_1^2$
p_{0v}^+ = dimensionless saturate vapor pressure = $p_{0v}/\rho_v v_1^2$
Δp_{cap} = capillary pressure head generated by the wick, Pa
Δp_l = overall liquid pressure drop along the heat pipe, Pa
Δp_v = overall vapor pressure drop along the heat pipe, Pa
Δp_l^+ = overall dimensionless liquid pressure drop along the heat pipe = $p_l^+ - p_{0v}^+$
Δp_v^+ = overall dimensionless vapor pressure drop along the heat pipe = $p_v^+ - p_{0v}^+$
$Q_{\max}$ = maximum input heat power under capillary limit, W
$q_{b,\max}$ = maximum heat flux for boiling limit, W/m^2
r, y = coordinates, m
r^+, y^+ = dimensionless coordinates; $r^+ = r\nu_v/h^2 v_1$, $y^+ = y/h$
r_n = nucleation radius of the vapor bubbles, m

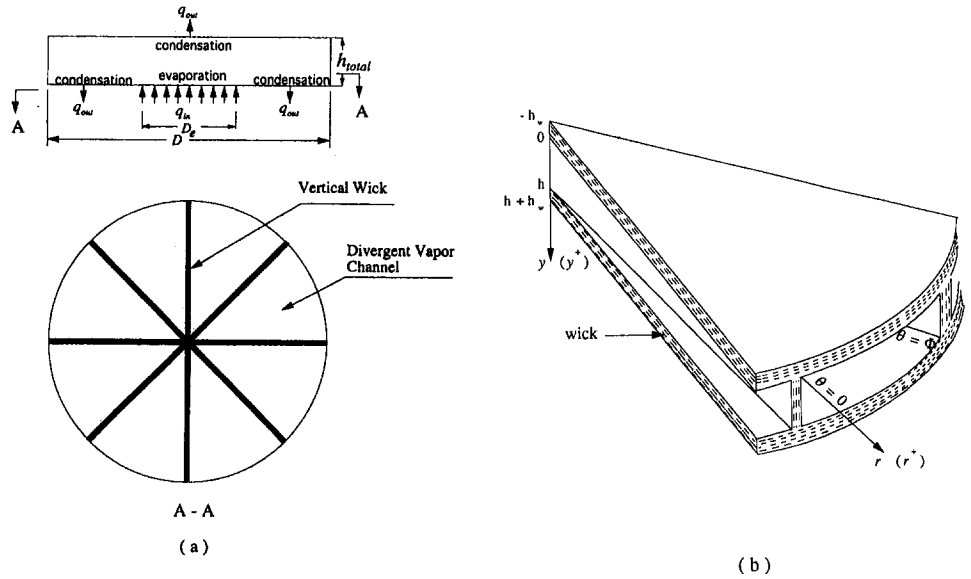

Fig. 1 Schematic of the disk-shaped heat pipe: (*a*) geometry of the heat pipe, (*b*) the coordinate system used in the analysis

where $\theta^+ = \theta/\Phi$. Since the angular component of $u_v^+(r^+, y^+, \theta^+)$ given by Eq. (8) is uncoupled from r^+ and y^+, the r^+ and y^+ component of $u_v^+(r^+, y^+, \theta^+)$ can be determined by concentrating only on the $r^+ - y^+$ plane. Therefore, the velocity profile in the $r^+ - y^+$ plane is

$$u_v^+(r^+, y^+) = U_v^+(r^+)[a_0 + a_1 y^+ + a_2 (y^+)^2]. \quad (9)$$

The vapor flow in the heat pipe does not have a symmetric velocity profile in the $r^+ - y^+$ plane. The location of the maximum vapor velocity will be shifted toward the upper plate due to the vapor injection from the heating side of the lower plate. As the vapor flows downstream, the location of the maximum velocity will gradually shift toward the centerline due to the presence of symmetric cooling conditions. To account for this feature, the velocity profile in y^+ direction will be divided into two parts based on the location of the maximum velocity (Fig. 2): the upper part ($0 \le y^+ \le f^+(r^+)$) and the lower part ($f^+(r^+) \le y^+ \le 1$). The location of the maximum velocity, $y^+ = f^+(r^+)$, is also the location corresponding to zero shear stress for the velocity distribution on the $r^+ - y^+$ plane. Applying boundary condition (4) and

$$u_v^+(r^+, f^+(r^+)) = U_v^+(r^+), \quad \left.\frac{\partial u_v^+(r^+, y^+)}{\partial y^+}\right|_{y^+ = f^+(r^+)} = 0$$

to Eq. (9) will result in the following velocity profiles:

$$u_v^+(r^+, y^+) = \begin{cases} U_v^+(r^+)\left[2\dfrac{y^+}{f^+(r^+)} - \left(\dfrac{y^+}{f^+(r^+)}\right)^2\right] \\ \quad (0 \le y^+ \le f^+(r^+)) \\ U_v^+(r^+)\left[2\left(\dfrac{1-y^+}{1-f^+(r^+)}\right) - \left(\dfrac{1-y^+}{1-f^+(r^+)}\right)^2\right] \\ \quad (f^+(r^+) \le y^+ \le 1). \end{cases} \quad (10)$$

Nomenclature (cont.)

r_w = porous radius of wick, m
R = radius of the disk-shaped heat pipe, m
R^+ = dimensionless radius of the disk-shaped heat pipe
$\bar{R}$ = ideal gas constant = 8.31433 kJ/(kmole·K)
Re_h = injection Reynolds number = $v_1 h/\nu_v$
T_v = vapor temperature, °C
T_v^+ = dimensionless vapor temperature = $T_v R/h_{fg}$
T_{0v}^+ = dimensionless saturate vapor temperature = $T_{0v} R/h_{fg}$
ΔT_v^+ = dimensionless vapor temperature drop along the heat pipe = $T_v^+ - T_{0v}^+$
u_l = liquid velocity, m/s
u_v = vapor velocity, m/s
u_l^+ = dimensionless liquid velocity = u_l/v_1
u_v^+ = dimensionless vapor velocity = u_v/v_1
U_v^+ = dimensionless vapor velocity component in r^+ direction
v_1 = vapor injection velocity, m/s
v_2 = vapor suction velocity, m/s
v_1^+ = dimensionless vapor injection velocity = $v_1 h/\nu_v$
v_2^+ = dimensionless vapor suction velocity = $v_2 h/\nu_v$
ϵ = wick porosity
θ = coordinate
θ^+ = dimensionless coordinate = θ/Φ
ν_l = kinematic viscosity of liquid, m^2/s
ν_v = kinematic viscosity of vapor, m^2/s
ν^+ = dimensionless kinematic viscosity = ν_l/ν_v
ρ_l = liquid density, kg/m^3
ρ_v = vapor density, kg/m^3
ρ^+ = dimensionless density = ρ_l/ρ_v
σ_l = surface tension of the working liquid, N/m
φ = square root of the ratio of the evaporator area to the heat pipe area; $\varphi^2 = A_e/\pi R^2$
Φ = angle of each divergent vapor channel of disk-shape heat pipe

Subscripts

e = evaporator
l = liquid phase
v = vapor phase
w = wick

Superscripts

$+$ = dimensionless quantities

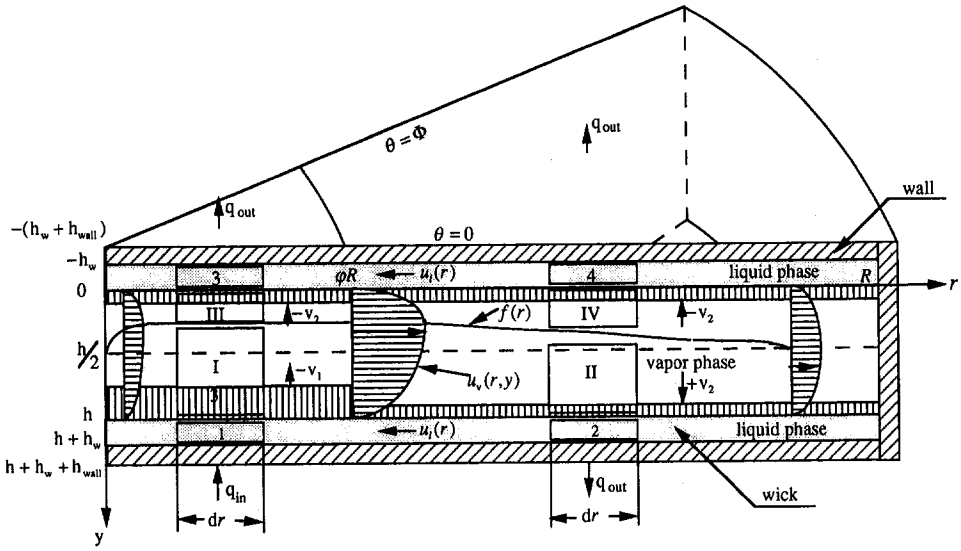

Fig. 2 Different regimes, which are analyzed for the vapor and liquid phases in the *r–y* plane of the heat pipe

The two unknowns $U_v^+(r^+)$ and $f^+(r^+)$ in Eq. (10) will be determined by integrating the continuity Eq. (1) and the momentum Eq. (2). Integrating the continuity Eq. (1) with respect to y^+ from 0 to 1 and substituting the velocity profile given by Eq. (10) into the integrated equation and applying boundary conditions given by Eqs. (4) and (6) will result in an expression for $U_v^+(r^+)$:

$$U_v^+(r^+) = \begin{cases} \dfrac{3(v_1^+ - v_2^+)}{4} r^+ & (0 \le r^+ \le \varphi R^+) \\ -\dfrac{3v_2^+}{2}\dfrac{1}{r^+}[(r^+)^2 - (R^+)^2] & (\varphi R^+ \le r^+ \le R^+). \end{cases} \quad (11)$$

As expected, $U_v^+(r^+)$ is related to vapor injection and suction velocities. Recognizing the fact that $U_v^+(r^+)$ must be continuous at $r^+ = \varphi R^+$ will result in

$$\varphi = \sqrt{\frac{2v_2^+}{v_1^+ + v_2^+}} \quad (12)$$

Using Eq. (12), Eq. (11) can be written as

$$U_v^+(r^+) = \begin{cases} \dfrac{3}{2}\dfrac{1-\varphi^2}{2-\varphi^2}\mathrm{Re}_h r^+ & (0 \le r^+ \le \varphi R^+) \\ -\dfrac{3}{2}\dfrac{\varphi^2}{2-\varphi^2}\dfrac{\mathrm{Re}_h}{r^+}[(r^+)^2 - (R^+)^2] & \\ (\varphi R^+ \le r^+ \le R^+). & \end{cases} \quad (13)$$

The $f^+(r^+)$ will be determined by integrating the r^+-momentum Eq. (2) with respect to y^+ for either the lower part or the upper part of the vapor space. It should be noted that in the $0 \le r^+ \le \varphi R^+$ region, there is a mass flow crossing the interface between the two control volumes I and III within the vapor phase (Fig. 2) due to the vapor injection from the lower wick and suction from the upper wick. However, in the $\varphi R^+ \le r^+ \le R^+$ region, due to the symmetric boundary conditions on both upper and lower wicks, there is no mass exchange between the two control volumes II and IV. Since the dimension in the r^+ direction is much larger than the transverse length in the vapor channel, the shear stress in the r^+ direction will be neglected (Narayana, 1986; Faghri, 1986). We have also been able to confirm that the shear stress in the r^+ direction is negligible when it was accounted for in the analysis. The above-mentioned considerations will result in the following set of equations for the upper part of the vapor space:

$$\frac{d}{dr^+}\int_0^{f^+(r^+)} (u_v^+(r^+, y^+, \theta^+))^2 dy^+ - U_v^+(r^+)J(\theta^+)\frac{d}{dr^+}\int_0^{f^+(r^+)} u_v^+(r^+, y^+, \theta^+)dy^+ + \int_0^{f^+(r^+)} \frac{1}{r^+}(u_v^+(r^+, y^+, \theta^+))^2 dy^+$$
$$- U_v^+(r^+)J(\theta^+)\int_0^{f^+(r^+)} \frac{1}{r^+} u_v^+(r^+, y^+, \theta^+)dy^+ - U_v^+(r^+)J(\theta^+)v_2^+ = -\int_0^{f^+(r^+)} \frac{\partial p_v^+}{\partial r^+} dy^+ + \int_0^{f^+(r^+)} \frac{\partial^2 u_v^+(r^+, y^+, \theta^+)}{\partial (y^+)^2} dy^+$$
$$- \frac{1}{\mathrm{Re}_h^2}\left[\int_0^{f^+(r^+)} \frac{u_v^+(r^+, y^+, \theta^+)}{(r^+)^2} dy^+ - \frac{1}{\Phi^2}\int_0^{f^+(r^+)} \frac{\partial^2 u_v^+(r^+, y^+, \theta^+)}{\partial (\theta^+)^2} dy^+\right] \quad (0 \le r^+ \le \varphi R^+) \quad (14a)$$

and

$$\frac{d}{dr^+}\int_0^{f^+(r^+)} (u_v^+(r^+, y^+, \theta^+))^2 dy^+ - (U_v^+(r^+))^2 (J(\theta^+))^2 \frac{df^+(r^+)}{dr^+} + \int_0^{f^+(r^+)} \frac{1}{r^+}(u_v^+(r^+, y^+, \theta^+))^2 dy^+$$
$$= -\int_0^{f^+(r^+)} \frac{\partial p_v^+}{\partial r^+} dy^+ + \int_0^{f^+(r^+)} \frac{\partial^2 u_v^+(r^+, y^+, \theta^+)}{\partial (y^+)^2} dy^+ - \frac{1}{\mathrm{Re}_h^2}\left[\int_0^{f^+(r^+)} \frac{u_v^+(r^+, y^+, \theta^+)}{(r^+)^2} dy^+ \right.$$
$$\left. - \frac{1}{\Phi^2}\int_0^{f^+(r^+)} \frac{\partial^2 u_v^+(r^+, y^+, \theta^+)}{\partial (\theta^+)^2} dy^+\right] \quad (\varphi R^+ \le r^+ \le R^+) \quad (14b)$$

where $J(\theta^+) = 4\theta^+(1-\theta^+)$. Using the vapor velocity profile and the average vapor pressure in each transverse plane in Eqs. (14*a*) and (14*b*) will result, after a very lengthy analysis, in the following expression for the rate of change of $f^+(r^+)$

$$\frac{df^+(r^+)}{dr^+} = \begin{cases} \left\{\left[\dfrac{2(1-\varphi^2)J(\theta^+)}{2-\varphi^2} + \dfrac{10}{3\,\mathrm{Re}_h^3(r^+)^2}\left(1+\dfrac{8}{\Phi^2 J(\theta^+)}\right)\right]f^+(r^+) + \dfrac{10}{\mathrm{Re}_h f^+(r^+)} - \dfrac{5\varphi^2}{2-\varphi^2} \right. \\ \left. + \dfrac{10(2-\varphi^2)f^+(r^+)}{3(1-\varphi^2)J(\theta^+)\,\mathrm{Re}_h^2 r^+}\dfrac{dp_v^+}{dr^+}\right\}\dfrac{2-\varphi^2}{(1-\varphi^2)J(\theta^+)r^+} \qquad (0 \le r^+ \le \varphi R^+) \\ \left\{\left[\dfrac{6\varphi^2 J(\theta^+)}{5(2-\varphi^2)}\left((r^+)^2+(R^+)^2\right) - \dfrac{1}{\mathrm{Re}_h^3}\left(1+\dfrac{8}{\Phi^2 J(\theta^+)}\right)\right]f^+(r^+) - \dfrac{3(r^+)^2}{\mathrm{Re}_h} - \dfrac{1}{f^+(r^+)} \right. \\ \left. + \dfrac{2-\varphi^2}{\varphi^2 J(\theta^+)}\dfrac{(r^+)^3}{(r^+)^2-(R^+)^2}\dfrac{f^+(r^+)}{\mathrm{Re}_h^2}\dfrac{dp_v^+}{dr^+}\right\}\dfrac{20(2-\varphi^2)}{21\varphi^2 J(\theta^+)r^+[(r^+)^2-(R^+)^2]} \qquad (\varphi R^+ \le r^+ \le R^+). \end{cases} \tag{15}$$

Since $U^+(0) = U^+(R^+) = 0$, and the velocity distributions at $r^+ = 0$ and $r^+ = R^+$ are uniform, the boundary conditions for the function $f^+(r^+)$ are taken as $f^+(0) = f^+(R^+) = 1/2$. The use of Eqs. (8), (10), (13), and (15) in Eq. (7) will provide us with the complete velocity profile within the disk-shaped heat pipe assembly.

(b) Pressure Distribution. The pressure distribution in the vapor phase can be obtained by integrating the r^+-momentum Eq. (2) within a channel bounded by porous wicks. Introducing continuity Eq. (1), the velocity profile given by Eqs. (8), (10), (13), and (15) and boundary conditions given by Eq. (6) into the integrated momentum equation will result, after a very lengthy analysis, in the following expression for the pressure gradient:

$$\frac{dp_v^+}{dr^+} = \begin{cases} -\dfrac{2(1-\varphi^2)}{(2-\varphi^2)}\mathrm{Re}_h\left\{\left[\dfrac{24}{25}\dfrac{(1-\varphi^2)}{(2-\varphi^2)}\mathrm{Re}_h + \dfrac{1}{f^+(1-f^+)}\right]r^+ + \dfrac{4}{\mathrm{Re}_h^2\Phi^2 r^+}\right\} \qquad (0 \le r^+ \le \varphi R^+) \\ -\dfrac{2\varphi^2}{(2-\varphi^2)}\mathrm{Re}_h\left\{\left[\dfrac{24}{25}\dfrac{\varphi^2}{(2-\varphi^2)}\mathrm{Re}_h - \dfrac{1}{f^+(1-f^+)}\right]r^+ - \dfrac{4}{\mathrm{Re}_h^2\Phi^2 r^+} + \dfrac{8}{25}\dfrac{\varphi^2\mathrm{Re}_h}{(2-\varphi^2)}\dfrac{(R^+)^2}{r^+}\right\}\dfrac{(r^+)^2-(R^+)^2}{(r^+)^2} \\ (\varphi R^+ \le r^+ \le R^+). \end{cases} \tag{16}$$

The coupled Eqs. (15) and (16) are solved by using the Runge–Kutta method for the pressure drop $\Delta p_v^+(r^+)$ and $f^+(r^+)$. A good approximation for the $f^+(r^+)$ is developed by using Bernoulli's equation at $y^+ = f^+(r^+)$ and is used as startup for the numerical calculations. The use of Bernoulli's equation will result in

$$\frac{df^+(r^+)}{dr^+} = \begin{cases} \left\{\left[-11(1-\varphi^2)J(\theta^+) + \dfrac{20(2-\varphi^2)}{3\,\mathrm{Re}_h^3(r^+)^2}\left(1+\dfrac{8}{J(\theta^+)\Phi^2}\right)\right]f^+(r^+) \right. \\ \left. + \dfrac{20(2-\varphi^2)}{\mathrm{Re}_h}\dfrac{1}{f^+(r^+)} - 10\varphi^2\right\}\dfrac{1}{(1-\varphi^2)J(\theta^+)r^+} \qquad (0 < r^+ \le \varphi R^+) \\ \left\{\left[(9(r^+)^2 - 7(R^+)^2)J(\theta^+) - \dfrac{20(2-\varphi^2)}{3\varphi^2\,\mathrm{Re}_h^3}\left(1+\dfrac{8}{J(\theta^+)\Phi^2}\right)\right]f^+(r^+) \right. \\ \left. - \dfrac{20(2-\varphi^2)}{\varphi^2\,\mathrm{Re}_h}\dfrac{(r^+)^2}{f^+(r^+)}\right\}\dfrac{1}{7J(\theta^+)r^+((r^+)^2-(R^+)^2)} \qquad (\varphi R^+ \le r^+ < R^+). \end{cases} \tag{17}$$

(c) Temperature Distribution. The vapor temperature distribution can be related to the vapor pressure distribution by using the Clausius–Clapeyron equation. In this work, the vapor is assumed to behave as an ideal gas and the volume of the liquid within the vapor phase is neglected (Winter and Barsch, 1971; Ivanovskii et al., 1982). The dimensionless temperature profile based on the Clausius–Clapeyron equation can be found from

$$\Delta T_v^+(r^+) = (T_{0v}^+)^2\left[\frac{\ln p_v^+(r^+) - \ln p_{0v}^+}{1 - T_{0v}^+(\ln p_{0v}^+ - \ln p_v^+(r^+))}\right] \tag{18}$$

where $T_{0v}^+ = T_{0v}/(h_{fg}/R)$ is the dimensionless saturation temperature.

2 Liquid Phase Analysis

(a) Velocity Profile. Since both upper and lower wicks in the $\varphi R^+ \le r^+ \le R^+$ region act as condensers, the condensate in both upper and lower wicks of the $\varphi R^+ \le r^+ \le R^+$ region (sections 4 and 2 of Fig. 2) flows directly toward section 3 and section 1, respectively, along the horizontal wicks. There is no liquid exchange through the vertical wicks in the $\varphi R^+ \le r^+ \le R^+$ region due to the symmetric boundary conditions. Therefore, the condensate will have only one velocity component, u_l^+, along the r^+ direction in the $\varphi R^+ \le r^+ \le R^+$ region. However, within the $0 \le r^+ \le \varphi R^+$ region the condensate in both upper and lower wicks possesses two distinct velocity components, u_l^+ in the r^+ direction and w_l^+ in the θ^+ direction, since the lower wick (evaporator) gets part of the liquid supply from the upper wick through the vertical wicks. Applying mass conservation for the condensate in both upper and lower wicks and eliminating w_l^+ by adding the lower and upper wick mass conservation equations together will result in the following equations for the velocity distribution in the r^+ direction:

$$\begin{cases} \dfrac{d(u_l^+(r^+))}{dr^+} + \dfrac{u_l^+(r^+)}{r^+} - \dfrac{v_l^+ - v_2^+}{2h_w^+\rho^+} = 0 \\ (0 \le r^+ \le \varphi R^+) \\ \dfrac{d(u_l^+(r^+))}{dr^+} + \dfrac{u_l^+(r^+)}{r^+} + \dfrac{v_2^+}{h_w^+\rho^+} = 0 \\ (\varphi R^+ \le r^+ \le R^+) \end{cases} \tag{19}$$

where $\rho^+ = \rho_l/\rho_v$ and $h_w^+ = h_w/h$. Solving Eq. (19) subject to the following boundary conditions:

$$u_l^+(0) = u_l^+(R^+) = 0$$

results in the liquid phase velocity distribution

$$u_l^+(r^+) = \begin{cases} \dfrac{v_l^+ - v_2^+}{4\rho^+ h_w^+} r^+ & (0 \le r^+ \le \varphi R^+) \\ -\dfrac{v_2^+}{2\rho^+ h_w^+} \dfrac{(r^+)^2 - (R^+)^2}{r^+} & \\ (\varphi R^+ \le r^+ \le R^+). & \end{cases} \tag{20}$$

The continuity of $u_l^+(r^+)$ at $r^+ = \varphi R^+$ will reconfirm the result given in Eq. (12).

(b) Pressure Distribution. The pressure distribution in the wick along the r^+ direction can be related to the liquid velocity distribution by Darcy's law. The dimensionless Darcy's law is

$$\frac{dp_l^+(r^+)}{dr^+} = \frac{1}{K^+} u_l^+(r^+) \tag{21}$$

where $K^+ = K/h_w^2$ is the dimensionless permeability. It should be noted that in using Darcy's law some important aspects related to boundary and inertial effects are neglected (Vafai and Tien, 1981; Tien and Vafai, 1989). Substituting Eq. (20) into Eq. (21) and using the boundary condition

$$p_l^+(R^+) = p_v^+(R^+)$$

will result in

$$p_l^+(r^+) = \begin{cases} p_v^+(R^+) + \dfrac{\nu^+}{4K^+(h_w^+)^3} \dfrac{\varphi^2 \mathrm{Re}_h}{(2-\varphi^2)} \left[\dfrac{1-\varphi^2}{\varphi^2}(r^+)^2 + 2(R^+)^2 \ln(\varphi) \right] & (0 \le r^+ \le \varphi R^+) \\ p_v^+(R^+) + \dfrac{\nu^+}{4K^+(h_w^+)^3} \dfrac{\varphi^2 \mathrm{Re}_h}{(2-\varphi^2)} \left[(R^+)^2 - (r^+)^2 - 2(R^+)^2 \ln\left(\dfrac{R^+}{r^+}\right) \right] & (\varphi R^+ \le r^+ \le R^+). \end{cases} \tag{22}$$

3 Maximum Heat Transfer Capability. There are limits on the maximum heat input that a heat pipe is capable of removing. For a low-temperature heat pipe usually only the boiling limit and capillary limit will be in effect (Tien, 1975). The maximum heat flux for boiling limit can be calculated as follows (Chi, 1976):

$$q_{b,\max} = \frac{k_e T_v}{\rho_v h_{fg} h_w} \left(\frac{2\sigma_l}{r_n} - \Delta p_{\mathrm{cap}} \right) \tag{23}$$

where k_e is the effective thermal conductivity of the liquid-saturated wick, σ_l the surface tension of the working liquid in the wick, r_n the nucleation radius of the vapor bubbles, and Δp_{cap} is the capillary pressure head. Assuming that there are no noncondensable gases within the heat pipe, the value of r_n can be taken as 2.54×10^{-7} m (Chi, 1976). Some typical values can be considered to evaluate the maximum heat flux for boiling limit. For example, for the heavy water heat pipe under current study, which operates at 80°C, the wick pore radius is taken as $r_w = 0.019$ cm, permeability $K = 1.8 \times 10^{-9}$ m^2, porosity $\varepsilon = 0.8$, and the effective thermal conductivity is taken as $k_e = 13.84$ W/mK. The maximum heat flux for boiling limit is then calculated as

$$q_{b,\max} = 1.85 \times 10^6 \text{ W/m}^2 = 185 \text{ W/cm}^2$$

This value is larger than the maximum heat transfer rate limited by the capillary limit. Thus we will concentrate on the capillary limit. For a heat pipe under steady-state operation, the capillary pressure head needed for the return of condensate from the condenser to the evaporator is balanced by the sum of total vapor pressure drop and total liquid pressure drop and gravitational pressure head; that is

$$\Delta p_{\mathrm{cap}} = \Delta p_{v,\mathrm{total}} + \Delta p_{l,\mathrm{total}} + \Delta p_{g,\mathrm{total}}. \tag{24}$$

The gravitational head $\Delta p_{g,\mathrm{total}}$ can be neglected for the horizontal heat pipe, and the overall vapor and liquid pressure drops are established as

$$\Delta p_{v,\mathrm{total}} = p_v(0) - p_v(R) \tag{25}$$

$$\Delta p_{l,\mathrm{total}} = p_l(R) - p_l(0), \tag{26}$$

Therefore, the capillary pressure head is presented as

$$\Delta p_{\mathrm{cap}} = \Delta p_{v,\mathrm{total}} + \Delta p_{l,\mathrm{total}} = p_v(0) - p_l(0). \tag{27}$$

When the input heat flux increases, the total pressure drops in both vapor and liquid regions increase; thus the capillary pressure head increases to meet the heat transfer and flow conditions. However, there exists a maximum capillary pressure head given by

$$\Delta p_{\mathrm{cap,max}} = \frac{2\sigma_l}{r_w} \tag{28}$$

where r_w is the capillary radius of the porous wick. If the capillary pressure head needed is larger than $\Delta p_{\mathrm{cap,max}}$, the heat pipe operation will dry out the wick. Therefore the heat that the disk-shaped or the flat-plate heat pipe transfers when it reaches the capillary limit is the maximum heat transfer, $Q_{\max}$. As long as $\Delta p_{\mathrm{cap,max}}$ is specified, $Q_{\max}$ can be determined according to this analysis. The maximum heat transfer capability per unit external surface area of the heat pipe is then determined based on $Q_{\max}$ and is discussed later.

4 Simplified Analytical Solution. Noticing that the values of the injection Reynolds number under current study are very large relative to other parameters, as an approximation we can neglect the affected terms in Eqs. (17) and reach the following expressions for $f^+(r^+)$:

$$f^+(r^+) = \begin{cases} -\dfrac{10\varphi^2 e^{-A/2(r^+)^2}}{(1-\varphi^2)J(\theta^+)(r^+)^{11}} \displaystyle\int (r^+)^{10} e^{A/2(r^+)^2} dr^+ \\ (0 \le r^+ \le \varphi R^+) \\ c(r^+)^{1+B}((R^+)^2 - (r^+)^2)^{(1/7-B/2)} \\ (\varphi R^+ \le r^+ \le R^+) \end{cases} \quad (29)$$

where

$$A = \frac{20(2-\varphi^2)}{3(1-\varphi^2)J(\theta^+)\,\mathrm{Re}_h^3}\left(1 + \frac{8}{J(\theta^+)\Phi^2}\right) \quad (30)$$

$$B = \frac{20(2-\varphi^2)}{21\varphi^2 J(\theta^+)\,\mathrm{Re}_h^3\,(R^+)^2}\left(1 + \frac{8}{J(\theta^+)\Phi^2}\right) \quad (31)$$

and c is the integration constant, which is determined by the continuous condition of $f^+(r^+)$ at $r^+ = \varphi R^+$. Similarly, Eq. (16) can be simplified to obtain the following expression for the vapor pressure:

Results and Discussion

The results based on this analysis for the disk-shaped heat pipe are presented and compared with those of square flat-plate heat pipe analyzed by Vafai and Wang (1992). To make the comparison meaningful at all times the diameter of the disk-shaped heat pipe is taken equal to the length of the square flat-plate heat pipe, i.e., $R = l$. On the same basis, the heat input areas (the evaporator section) and the values of h and h_w for both disk-shaped and square flat-plate heat pipes are taken to be equal. Comparisons between the performance of the disk-shaped and the square flat-plate heat pipes as a function of h, h_w, and R (or l) are presented later. The respective dimensions of the heat pipes, based on our application, are chosen as: $R = l = 0.46$ m, $h = 0.0254$ m, and $h_w = 2 \times 10^{-3}$ m. The working fluid is heavy water, which has the following thermophysical properties: $h_{fg} = 2128$ kJ/kg, $\rho_v = 0.3055$ kg/m^3, $\rho_l = 1078.3$ kg/m^3, $\mu_v = 1.1876 \times 10^{-5}$ Ns/m^2, and $\mu_l = 41.6 \times 10^{-5}$ Ns/m^2. The results for both disk-shaped and square flat-plate heat pipes have been calculated for Re_h values of 250, 750, and 1000, which corresponds to the input heat powers of 46.25 kW, 92.5 kW, and 185 kW,

$$p_v^+(r^+) = \begin{cases} p^+(0) - \dfrac{24}{25}\left(\dfrac{1-\varphi^2}{2-\varphi^2}\mathrm{Re}_h R^+\right)^2\left(\dfrac{r^+}{R^+}\right)^2 \quad (0 \le r^+ \le \varphi R^+) \\ p_v^+(0) - \dfrac{8}{25}\left(\dfrac{\varphi^2}{2-\varphi^2}\mathrm{Re}_h R^+\right)^2\left[3\left(\dfrac{r^+}{R^+}\right)^2 + \left(\dfrac{R^+}{r^+}\right)^2 - 4\ln\dfrac{r^+}{R^+} - 2\left(3 - 2\ln\varphi - \dfrac{1}{\varphi^2}\right)\right] \\ (\varphi R^+ \le r^+ \le R^+) \end{cases} \quad (32)$$

The liquid pressure profile is therefore given as follows:

$$p_l^+(r^+) = \begin{cases} p_v^+(0) + \dfrac{\nu^+\,\mathrm{Re}_h\,(R^+)^2}{4K^+(h_w^+)^3}\dfrac{1-\varphi^2}{2-\varphi^2}\left[\left(\dfrac{r^+}{R^+}\right)^2 + \dfrac{2\varphi^2}{1-\varphi^2}\ln\varphi\right] - \left(\dfrac{4}{5}\dfrac{\varphi^2\,\mathrm{Re}_h}{2-\varphi^2}R^+\right)^2\left(2\ln\varphi + \dfrac{1}{\varphi^2} - 1\right) \\ (0 \le r^+ \le \varphi R^+) \\ p_v^+(0) + \dfrac{\nu^+\,\mathrm{Re}_h\,(R^+)^2}{4K^+(h_w^+)^3}\dfrac{\varphi^2}{2-\varphi^2}\left[1 - \left(\dfrac{r^+}{R^+}\right)^2 - 2\ln\left(\dfrac{R^+}{r^+}\right)\right] - \left(\dfrac{4}{5}\dfrac{\varphi^2\,\mathrm{Re}_h}{2-\varphi^2}R^+\right)^2\left(2\ln\varphi + \dfrac{1}{\varphi^2} - 1\right) \\ (\varphi R^+ \le r^+ \le R^+) \end{cases} \quad (33)$$

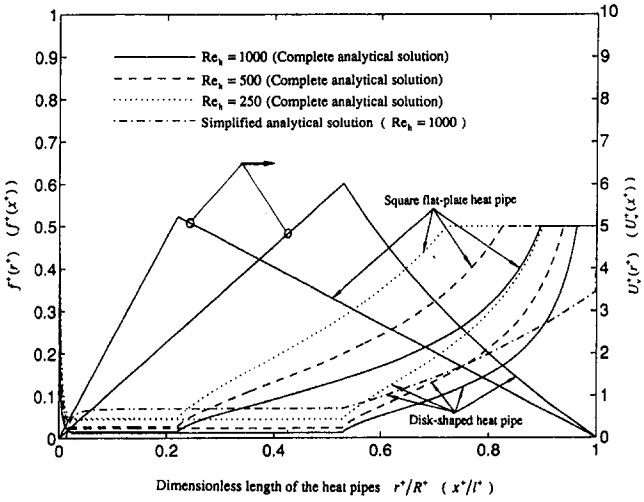

Fig. 3 Variations of the maximum vapor velocity and its location along heat pipe channels

respectively. It is important to note that due to the analytical nature of the solution, various ranges of the pertinent parameters along with different heat pipe sizes can be readily analyzed.

Figure 3 shows the variation of the maximum vapor velocity $U_v^+(r^+)$ [$U_v^+(x^+)$ for the square flat-plate heat pipe] along the r^+ axis [x^+ axis for the square flat-plate heat pipe]. As mentioned earlier, to have meaningful comparisons the heat input areas (the evaporator area) for both disk-shaped and square flat-plate heat pipes were selected to be equal. This obviously will translate to different φ values for the disk-shaped and the square flat-plate heat pipes. For both disk-shaped and square flat-plate heat pipes, vapor accelerates in the $0 \le r^+ \le \varphi R^+$ [$0 \le x^+ \le \varphi l^+$] region corresponding to the evaporator section and decelerates in the $\varphi R^+ \le r^+ \le R^+$ [$\varphi l^+ \le x^+ \le l^+$] region corresponding to the condenser section, due to the vapor injection and suction over the corresponding regions. The acceleration within evaporator section of the disk-shaped heat pipe is smaller than that of the square flat-plate heat pipe, and the deceleration within condenser section of the disk-shaped heat pipe is larger than that of the square flat-plate heat pipe. This is because the rate of increase of the net vapor mass flow within the evaporator section of the disk-shaped heat pipe is smaller than that of the square flat-plate heat pipe; and the rate of decrease of the net vapor mass flow within

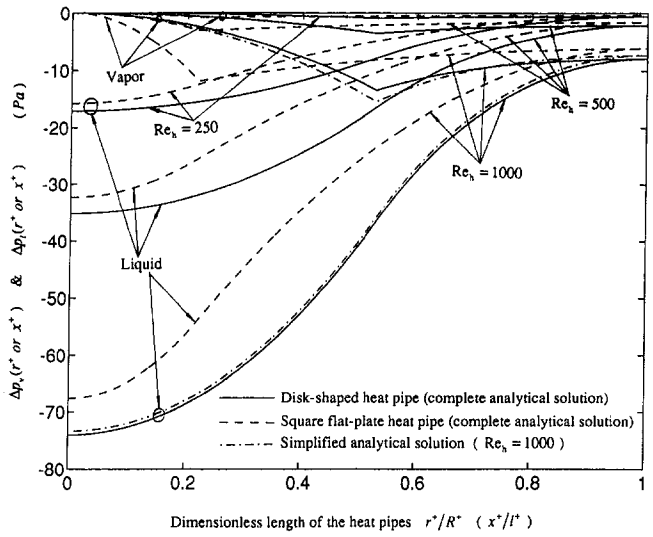

Fig. 4 Vapor and liquid pressure distributions for both disk-shaped and square flat-plate heat pipes

the condenser section of the disked-shaped heat pipe is larger than that of the square flat-plate heat pipe, due to the divergent vapor channel and the larger suction velocity of the disk-shaped heat pipe.

The locations of the maximum vapor velocity for both the disk-shaped heat pipe, $f^+(r^+)$, and the square flat-plate heat pipe, $f^+(x^+)$, are also shown in Fig. 3 and compared to each other. As expected, the location of the maximum vapor velocity is shifted toward the cooling side of either disk-shaped or flat-plate heat pipe in the $0 \le r^+ \le \varphi R^+$ [$0 \le x^+ \le \varphi l^+$] region while it returns to the center line of the heat pipe in the $\varphi R^+ \le r^+ \le R^+$ [$\varphi l^+ \le x^+ \le l^+$] region. For larger values of Re_h, the location of the maximum vapor velocity is shifted more prominently toward the cooling side, and it takes longer in the $\varphi R^+ \le r^+ \le R^+$ [$\varphi l^+ \le x^+ \le l^+$] region to return to the centerline. This is due to the fact that for larger input heat fluxes, larger amounts of vapor mass need to be condensed. The simplified analytical solution for $\mathrm{Re}_h = 1000$ is also shown in this figure.

For the disk-shaped heat pipe, $f^+(r^+)$ is pulled a little closer to the cooling side and takes a relatively shorter distance in the $\varphi R^+ \le r^+ \le R^+$ region to return to the centerline. This is because both heat pipes have the same value of injection velocity v_1^+, but the disk-shaped heat pipe has a larger suction velocity v_2^+ since it has less surface area than the square flat-plate heat pipe. Furthermore, although the distances from $r^+ = \varphi R^+$ [$x^+ = \varphi l^+$] to the location where $f^+(r^+)$ [$f^+(x^+)$] returns to the center line are different for disk-shaped and square flat-plate heat pipes, our results have demonstrated that the amounts of vapor mass sucked within these distances are the same for both heat pipes at a given value of Re_h. For example, for $\mathrm{Re}_h = 1000$, the injection velocity is $v_1 = 1.53$ m/s for both disk-shaped and square flat-plate heat pipes, but the suction velocities will be $v_2 = 0.2487$ m/s for the disk-shaped heat pipe and $v_2 = 0.1887$ m/s for the square flat-plate heat pipe. The surface areas needed for $f^+(r^+)$ ($f^+(x^+)$) to return to the centerline are $a = 0.4306$ m^2 for the disk-shaped heat pipe and $a = 0.5721$ m^2 for the square flat-plate heat pipe. Therefore the condensed mass flow rates within these surface areas are the same for both disk-shaped and square flat-plate heat pipes and given by $\rho a v_2 = 0.0165$ kg/s. This means for the same input heat power and the same evaporator surface area A_e, i.e., for the same input heat flux, the disk-shaped heat pipe will condense the vapor mass more efficiently with less cooling surface than the larger square flat-plate heat pipe.

Figure 4 shows the vapor and liquid pressure distributions for both disk-shaped and square flat-plate heat pipes, where $\Delta p_v(r) = p_v(r) - p_v(0)$ and $\Delta p_l(r) = p_l(r) - p_v(0)$. As in conventional heat pipes, there is a vapor pressure drop in the evaporator region due to vapor acceleration in that region and a vapor pressure recovery in the condenser region due to the vapor deceleration in that region. The larger the injection Reynolds number, the larger the vapor and liquid pressure drops. Compared to the square flat-plate heat pipe, the vapor pressure of disk-shaped heat pipe decreases more slowly in the evaporator region and increases faster in the condenser region due to its smaller vapor acceleration within evaporator region and larger vapor deceleration within condenser region. This is in agreement with the maximum vapor velocity distribution shown in Fig. 3. The overall liquid pressure drop for the disk-shaped heat pipe is a little larger than that of the square flat-plate heat pipe. This is because of the convergence of the liquid flow channel, which leads to a larger capillary pressure head for the disk-shaped heat pipe. The simplified analytical solution for $\mathrm{Re}_h = 1000$ is also shown in this figure.

Figure 5 shows the vapor temperature distribution along the heat pipes. The temperature distribution is given relative to the saturation temperature T_{0v}^+, which is the temperature when the effect of the vapor pressure drop is neglected, in the form of $\Delta T_v^+ = T_v^+ - T_{0v}^+$. As shown in Fig. 5, there is a vapor temperature drop in the evaporator region and a temperature recovery in the condenser region due to the effect of vapor pressure drop. This is consistent with the numerical and experimental results of conventional cylindrical heat pipes reported by Tien and Rohani (1974) and Busse (1973). For both disk-shaped and square flat-plate heat pipes, the vapor temperature is quite uniform ($\Delta T \ll 1$°C). This demonstrates the successful operation of both of these heat pipes for high input heat fluxes encountered in such applications as that of BNCT.

Figure 6 shows the effects of variations in the thickness of the wick and the vapor channel as well as the overall thickness of the heat pipe on the maximum heat input power that can be transferred per unit surface area by both types of heat pipes. In this figure as well as in Fig. 7, A_{total} refers to the total external area of each heat pipe and h_{total} is the thickness of each heat pipe, $h_{\text{total}} = h + 2h_w$. Figure 6($a$) presents $Q_{\max}/A_{\text{total}}$ as a function of the wick thickness, while Fig. 6(b) shows $Q_{\max}/A_{\text{total}}$ as a function of the vapor channel thickness. Figure 6(c) shows $Q_{\max}/A_{\text{total}}$ as a function of the total thickness of the heat pipe, h_{total}. As expected, $Q_{\max}/A_{\text{total}}$ increases with an increase in h_{total} for a fixed value of h_w/h_{total}. In both Figs. 6(a) and 6(b), h_{total} is fixed as a constant for both types of heat pipe. It should be noted that the results in Figs. 6(a) and 6(b) were calculated independently. As seen in Fig. 6, there is an optimum value of h_w/h_{total} [Fig. 6(a)]

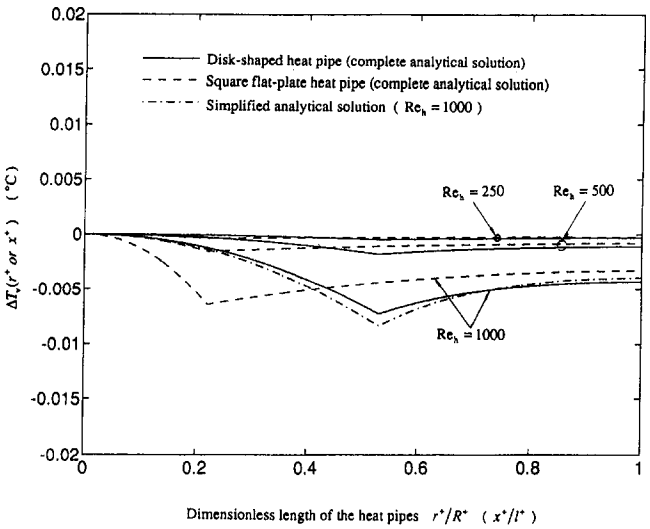

Fig. 5 Vapor temperature distributions for both disk-shaped and square flat-plate heat pipes

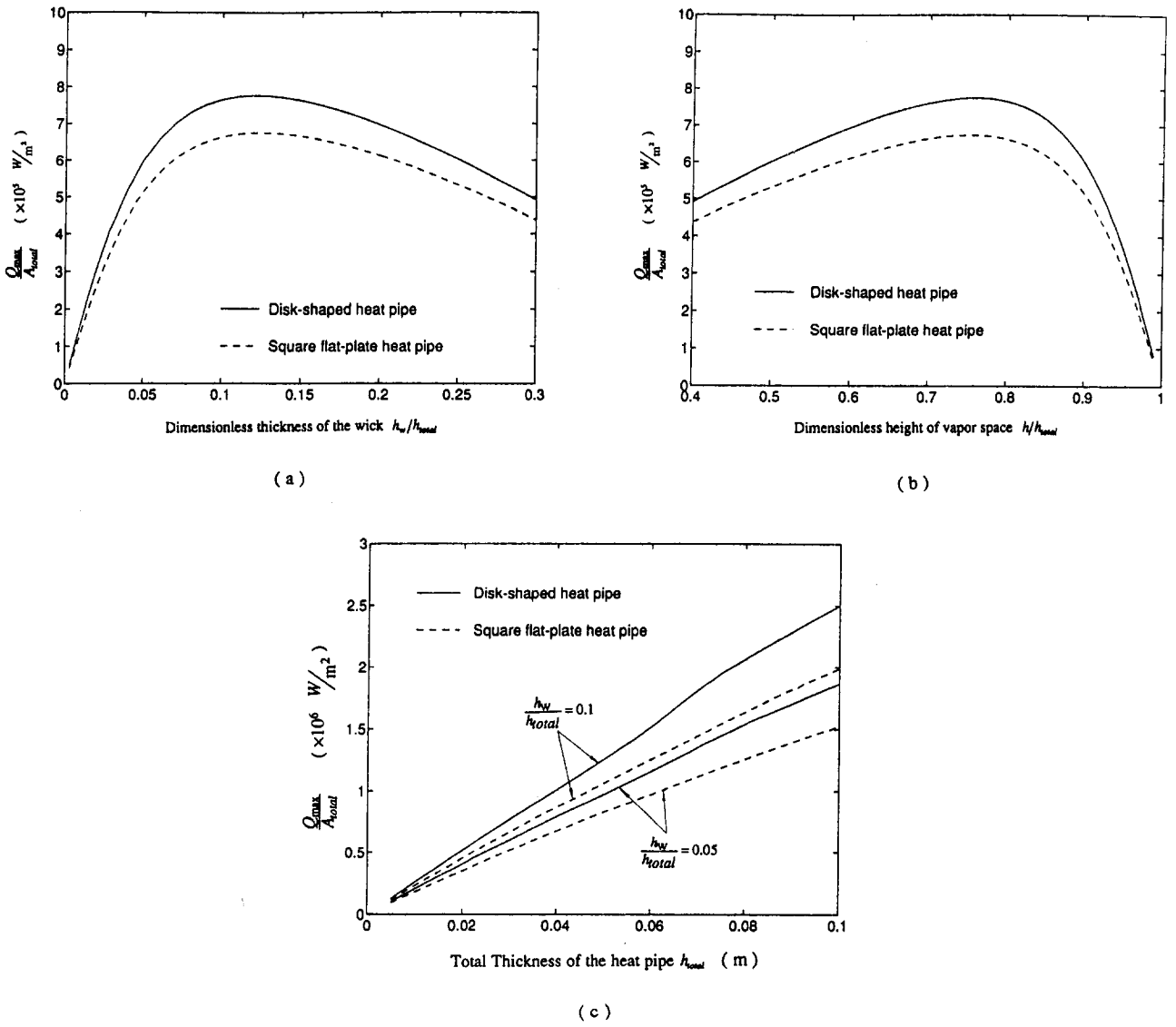

Fig. 6 Variations of maximum heat transfer per unit surface area as a function of (*a*) wick thickness, (*b*) thickness of the vapor space, (*c*) total thickness of the heat pipe

and an optimum value of h/h_{total} [Fig. 6(b)] at which $Q_{\max}/A_{\text{total}}$ reaches its maximum value. The values of h_w in these two optimum cases are exactly the same ($h_w = 0.12h_{\text{total}}$), and the difference between the corresponding values of $Q_{\max}/A_{\text{total}}$ from each figure is less than 0.001 percent. This demonstrates that for a given heat pipe thickness there exists a wick thickness relating to the optimum performance of the disk-shaped or flat-plate heat pipe.

Figure 7 shows the maximum heat transfer per unit surface area as a function of the total length of each type of heat pipe while h_{total} is fixed as a constant. As seen in Fig. 7(a), $Q_{\max}/A_{\text{total}}$ increases as h_w/h_{total} increases. However, after h_w/h_{total} reaches a certain value, $Q_{\max}/A_{\text{total}}$ decreases as h_w/h_{total} increases [Fig. 7(b)]. This reconfirms that there is an optimum wick thickness, which gives the maximum $Q_{\max}/A_{\text{total}}$ for both disk-shaped and square flat-plate heat pipes, as demonstrated in Figs. 6(a) and 6(b). Furthermore, it can be seen that for any length heat pipe the $Q_{\max}/A_{\text{total}}$ of the disk-shaped heat pipe is about 20 percent larger than that of the square flat-plate heat pipe, despite the smaller total external surface area of the disk-shaped heat pipe compared to that of the square flat-plate heat pipe.

The simplified analytical solution for the disk-shaped heat pipe is also presented (Figs. 3, 4, and 5). It can be seen that there is a relatively good agreement between the simplified analytical solution and the complete analytical solution for large injection Reynolds numbers. It should be noted that this simplified analytical solution does neglect some physical features. Nevertheless, it does provide us with a reasonable expression over a good portion of the heat pipe.

Conclusions

The vapor and liquid velocity and pressure distributions in an asymmetric disk-shaped heat pipe have been analyzed in depth in this work and analytical solutions for these quantities have been presented. The conceptual design and intrawick interactions for the disk-shaped heat pipe have been investigated in detail. The overall performance of both disk-shaped and square flat-plate heat pipes and the factors limiting their performance have been analyzed and the maximum heat transfer capability for both types of heat pipes with different sizes have been established. The effects of variations in the wick thickness and the vapor channel thickness as well as the overall thickness of the heat pipe on the performance of both types of heat pipes have been analyzed. The results show that the disk-shaped heat pipe, while utilizing a smaller surface area, significantly increases the heat transfer capability compared to the flat-plate heat pipe.

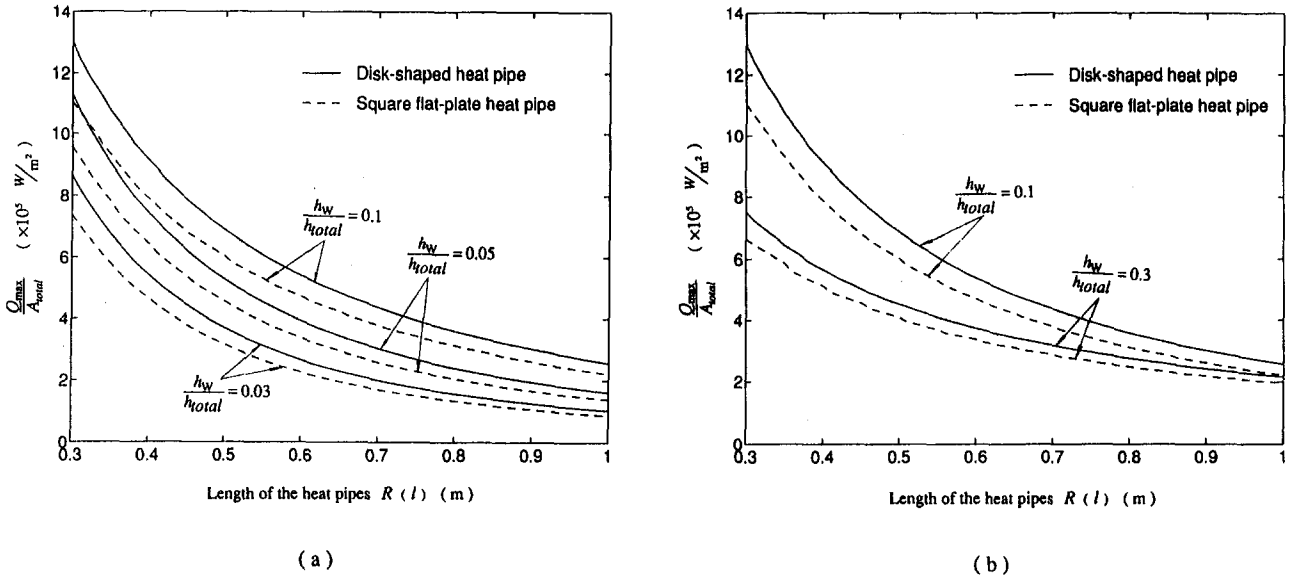

Fig. 7 Variations of maximum heat transfer per unit surface area as a function of the total length of the heat pipe

References

Bankston, C. A., and Smith, H. J., 1973, "Vapor Flow in Cylindrical Heat Pipes," ASME JOURNAL OF HEAT TRANSFER, Vol. 95, pp. 371–376.

Busse, C. A., 1973, "Theory of the Ultimate Heat Transfer Limit of Cylindrical Heat Pipes," *Int. J. Heat Mass Transfer,* Vol. 16, pp. 169–186.

Chen, M. M., and Faghri, A., 1990, "An Analysis of the Vapor Flow and the Heat Conduction Through the Liquid-Wick and Pipe Wall in a Heat Pipe With Single or Multiple Heat Sources," *Int. J. Heat Mass Transfer,* Vol. 33, pp. 1945–1955.

Chi, S. W., 1976, *Heat Pipe Theory and Practice,* McGraw-Hill, New York, pp. 89–95.

Dunn, P. D., and Reay, D. A., 1982, *Heat Pipes,* 3rd ed., Pergamon Press, New York.

Faghri, A., 1986, "Vapor Flow Analysis in a Double-Walled Concentric Heat Pipe," *Numerical Heat Transfer,* Vol. 10, pp. 583–595.

Horner-Richardson, K. D., 1991, "Heat Pipe Furnace Element and Epitaxy Susceptor Development," *Thermacore, Inc. Final Report to Electronic Systems Division,* Air Force Systems Command, USAF, Hanscom AFB, MA017311.

Ivanovskii, M. N., Sorokin, I. V., 1982, *The Physical Principles of Heat Pipes,* Clarendon Press, Oxford–New York.

Maezawa, S., Suzuki, Y., and Tsuchida, A., 1981, "Heat Transfer Characteristics of Disk-Shaped Rotating, Wickless Heat Pipe," *Proc. IV Int. Heat Pipe Conference,* Pergamon Press, Oxford, United Kingdom, pp. 725–733.

Narayana, K. B., 1986, "Vapor Flow Characteristics of Slender Cylindrical Heat Pipes—a Numerical Approach," *Numerical Heat Transfer,* Vol. 10, pp. 79–93.

Ooijen, H., and Hoogendoorn, C. J., 1979, "Vapor Flow Calculations in a Flat-Plate Heat Pipe," *AIAA Journal,* Vol. 17, pp. 1251–1259.

Rosenfeld, J. H., 1987, "Modeling of Heat Transfer Into a Heat Pipe for a Localized Heat Input Zone," *AIChE Symposium Series,* No. 257, Vol. 83, pp. 71–76.

Sorour, M. M., Hassab, M. A., and Estafanous, S., 1987, "Developing Laminar Flow in a Semi-porous Two Dimensional Channel With Nonuniform Transpiration," *Int. J. Heat Fluid Flow,* Vol. 8, pp. 44–53.

Tien, C. L., and Rohani, A. R., 1974, "Analysis of the Effect of Vapor Pressure Drop on Heat Pipe Performance," *Int. J. Heat Mass Transfer,* Vol. 17, pp. 61–67.

Tien, C. L., 1975, "Fluid Mechanics of Heat Pipes," *Annular Review of Fluid Mechanics,* Vol. 7, pp. 167–185.

Tien, C. L., and Vafai, K., 1989, "Convective and Radiative Heat Transfer in Porous Media," *Advances in Applied Mechanics,* Vol. 27, pp. 225–282.

Vafai, K., and Tien, C. L., 1981, "Boundary and Inertia Effects on Flow and Heat Transfer in Porous Media," *Int. J. Heat Mass Transfer,* Vol. 24, pp. 195–203.

Vafai, K., and Wang, W., 1992, "Analysis of Flow and Heat Transfer Characteristics of an Asymmetrical Flat Plate Heat Pipe," *Int. J. Heat Mass Transfer,* Vol. 35, pp. 2087–2099.

Winter, E. R. F., and Barsch, W. O., 1971, "The Heat Pipe," *Advances in Heat Transfer,* Vol. 7, pp. 219–320.